



# Effect of Ag doping on structural, optical and electrical properties of antimony sulfide thin films

C. J. Diliegros-Godines<sup>1</sup> , J. Santos Cruz<sup>2</sup> , N. R. Mathews<sup>3</sup> , and Mou Pal<sup>1,\*</sup>

<sup>1</sup>Instituto de Física, BUAP, Av. San Claudio y Blvd. 18 Sur Col. San Manuel, Ciudad Universitaria, C.P. 72570 Puebla, Mexico

<sup>2</sup>Facultad de Química, Materiales-Energía, Universidad Autónoma de Querétaro, C.P. 76101 Santiago de Querétaro, Qro, Mexico

<sup>3</sup>Instituto de Energías Renovables, Universidad Nacional Autónoma de México, 62580 Temixco, Morelos, Mexico

Received: 19 February 2018

Accepted: 8 May 2018

Published online:

16 May 2018

© Springer Science+Business Media, LLC, part of Springer Nature 2018

## ABSTRACT

This work reveals the effect of silver doping on structural, optical and electrical properties of  $\text{Sb}_2\text{S}_3$  films grown by a citrate-mediated chemical bath deposition technique. The silver content in solution was 7.5 mol% with respect to  $\text{Sb}^{3+}$  ions. The films were deposited in a cold bath for four hours and subjected to thermal treatment in a  $\text{N}_2$  atmosphere at 300 °C for 1 h. Polycrystalline nature of  $\text{Sb}_2\text{S}_3$  films with orthorhombic phase was confirmed in both undoped and Ag-doped samples by X-ray diffraction technique and Raman spectroscopy. Scanning electron microscopy imaging showed the presence of irregular-shaped interconnected particulate grains in the undoped films, while nearly spherical clusters of smaller grain size were observed for Ag-doped  $\text{Sb}_2\text{S}_3$  films. X-ray photoelectron spectroscopy results revealed the incorporation of metallic Ag into the  $\text{Sb}_2\text{S}_3$  lattice. A detailed growth mechanism has been proposed for the formation of  $\text{Sb}_2\text{S}_3$  and incorporation of metallic silver in the host matrix. The optical properties were recorded by UV–Vis diffuse reflectance spectroscopy. The inclusion of Ag in  $\text{Sb}_2\text{S}_3$  films causes a red shift in band gap values from 1.75 to 1.66 eV. The dark resistivity of  $\text{Sb}_2\text{S}_3$  films was decreased by one order on silver doping.

## Introduction

Among the binary chalcogenides, antimony sulfide thin films attract good expectations to the researchers due to their attractive photosensitivity and thermoelectric properties, large dielectric constant, high refractive index and air-stability [1–4]. In addition to low toxicity and natural abundance of its constituent elements,  $\text{Sb}_2\text{S}_3$  has high absorption coefficient

( $> 10^5 \text{ cm}^{-1}$ ) and direct optical band gap in the range of 1.6–2.2 eV [5] making them potential absorber material for harvesting solar energy in different types of solar cells such as thin film photovoltaics [6], Schottky diodes [7], semiconductor-sensitized solar cell [8, 9] and hybrid organic-inorganic extremely thin absorber solar cells [10, 11]. Recently, DeAngelis et al. have demonstrated the potential of  $\text{Sb}_2\text{S}_3$  thin films as a photoanode material in photocatalytic

Address correspondence to E-mail: mou@ifuap.buap.mx

water splitting [12]. The use of  $\text{Sb}_2\text{S}_3$  thin films in Pt-n $\text{Sb}_2\text{S}_3$  Schottky barrier solar cells has been illustrated with efficiency, ( $\eta$ ) of  $\sim 5.5\%$  [7]. A number of relevant research has been reported on  $\text{Sb}_2\text{S}_3$ -based semiconductor-sensitized solar cells comprised of FTO/ $\text{TiO}_2$ / $\text{Sb}_2\text{S}_3$ /hole conductor/Au yielding a power conversion efficiency of 6.5% [13]. In photovoltaics, the electrical resistivity of the active layer is one of the major concerns along with several additional important criteria such as effective absorption of incident photon and ability to collect the photo-generated carriers before they recombine. The resistivity of  $\text{Sb}_2\text{S}_3$  at room temperature is very high of the order of  $10^8$ – $10^9$   $\Omega$ -cm which restricts its use as buffer layer in photovoltaics [14]. One way to improve the resistivity is by doping with foreign atoms. So far, few attempts have been made in doping  $\text{Sb}_2\text{S}_3$  films with foreign atoms: Ag doping by Salim et al. and Dong et al. using chemical bath deposition and radio frequency sputtering respectively [15, 16], Sn-doping by Mushtaq et al. [17] by CBD method, C-doping by Cardenas et al. [18] by CBD, and Ni-doping by Mushtaq et al. [19] by CBD technique. Incorporation of Ag atoms in  $\text{Sb}_2\text{S}_3$  is found to be advantageous as the intrinsic high resistivity of  $\text{Sb}_2\text{S}_3$  films can be lowered as reported by Mitkova et al. [20]. In addition, silver doping is found to increase the refractive index of  $\text{Sb}_2\text{S}_3$  films which makes attractive its application in photonics [21]. A major difficulty for an effective doping of  $\text{Sb}_2\text{S}_3$  material with Ag ions is due to the large contrast in ionic radii of silver and antimony ions (ionic radii of  $\text{Sb}^{3+} = 0.74$  Å and  $\text{Ag}^+ = 1.26$  Å) and the charge difference between  $\text{Ag}^+$  and  $\text{Sb}^{3+}$  which are expected to cause a lattice distortion and charge re-compensation process in host matrix, producing a significant change in structural, optical and electronic properties.

In the present work, undoped and silver-doped  $\text{Sb}_2\text{S}_3$  thin films were developed by a citrate-mediated chemical bath deposition method. To the best of our knowledge, the use of sodium citrate as complexing agent in the deposition of  $\text{Sb}_2\text{S}_3$  films by CBD method has not been reported so far. The structural, optical and electrical properties of undoped and Ag-doped films were studied using X-ray diffraction (XRD), Raman scattering, scanning electron microscopy (SEM), energy-dispersive X-ray spectroscopy (EDS), X-ray photoelectron spectroscopy (XPS), UV–Vis spectroscopy and photoresponse study. Both undoped and Ag-doped  $\text{Sb}_2\text{S}_3$  thin films revealed

orthorhombic stibnite phase. A red shift in absorption edge and consequently a lower optical band gap were determined for Ag-doped  $\text{Sb}_2\text{S}_3$  compared to the undoped film. The resistivity of  $\text{Sb}_2\text{S}_3$  films was found to improve by one order due to Ag doping.

## Experimental section

### Materials

All chemical are commercially available and were used as received. The reagents used for the preparation of undoped and silver-doped  $\text{Sb}_2\text{S}_3$  thin films were as follows: antimony (III) chloride ( $\text{SbCl}_3$ , Sigma-Aldrich, 99%), ethylene glycol ( $\text{C}_2\text{H}_6\text{O}_2$ , J. T. Baker, 99.97%), sodium citrate tribasic dihydrate ( $\text{C}_6\text{H}_5\text{O}_7\text{Na}_3 \cdot 2\text{H}_2\text{O}$ , Sigma-Aldrich, 99%), sodium thiosulfate 5-hydrate ( $\text{Na}_2\text{S}_2\text{O}_3 \cdot 5\text{H}_2\text{O}$ , J. T. Baker, 99.5%), silver nitrate ( $\text{AgNO}_3 \cdot 2\text{H}_2\text{O}$ , Sigma-Aldrich, 99%) and Millipore water (18  $\Omega$ ).

### Preparation of $\text{Sb}_2\text{S}_3$ films

Antimony sulfide thin films were prepared by chemical bath deposition method using sodium citrate as a complexing agent. The chemical bath was prepared by dissolving 650 mg of  $\text{SbCl}_3$  in 8 mL of ethylene glycol. This was followed by the addition of 1 mL of 1 M trisodium citrate solution under stirring. A milky white solution was formed due to the complexation of  $\text{Sb}^{3+}$  ions with citrate ions. Subsequently, 25 mL of 1 M  $\text{Na}_2\text{S}_2\text{O}_3$  solution was added which was previously cooled at 10 °C prior to the addition. The whole mixture became transparent after the addition of thiosulfate solution. Finally, the total volume was adjusted to 100 mL by adding cold deionized water and stirred thoroughly. For the deposition of  $\text{Sb}_2\text{S}_3$ , clean microscopic glass substrates were placed vertically in the bath supported on the wall of the beaker. The deposition was carried out at 10 °C in order to avoid immediate precipitation and to assure a good adhesion of  $\text{Sb}_2\text{S}_3$  layer on the substrates. In our study, the optimal growth time for  $\text{Sb}_2\text{S}_3$  deposition was found to be 4 h. At the end of deposition, substrates coated with orange yellow films were taken out from the bath, washed with deionized water and dried under  $\text{N}_2$  flow. For the preparation of Ag-doped  $\text{Sb}_2\text{S}_3$  thin films, 37.23 mg of  $\text{AgNO}_3$  (corresponding to 7.5 mol% with respect to

Sb precursor) was dissolved in 2.5 mL of deionized water and was added to citrate complexed  $\text{Sb}^{3+}$  solution prior to the addition of sodium thiosulfate solution. Upon the addition of  $\text{AgNO}_3$ , the bath solution turned into highly viscous white mixture which became transparent after adding thiosulfate solution. The rest of the experimental parameters were kept similar as described earlier. In all the cases, thin film on one side of the substrate facing the wall of the beaker was retained to study the structural, optical and electrical properties, while the coating on the other side was removed by cotton swabs moistened with dilute HCl (1%). In order to induce crystallinity, the undoped and Ag-doped  $\text{Sb}_2\text{S}_3$  films were annealed in a vacuum furnace at 300 °C for 1 h in a tubular vacuum furnace (MTI-1200 OTF) under a nitrogen pressure of 1 atm.

## Characterization

The thickness of the undoped and Ag-doped  $\text{Sb}_2\text{S}_3$  films was determined by surface profilometer (Dektak 150) and found to increase from 612 to 670 nm on doping. The crystal structure of  $\text{Sb}_2\text{S}_3$  thin films was characterized by X-ray diffraction using a Bruker D8 Discover diffractometer with monochromatized  $\text{Cu-K}\alpha$  radiation ( $\lambda = 1.5406 \text{ \AA}$ ). The scanning was done in the  $2\theta$  range of 10°–80° at 40 kV and 40 mA. Raman scattering measurements were performed by means of confocal micro-Raman equipment (Jobin Yvon RAM HR800) focusing 632.8 nm line of He-Ne laser on  $\text{Sb}_2\text{S}_3$  films through 50X objective of a microscope (Olympus BX41). The optical reflectance spectra of the films were recorded in the wavelength range of 300–1200 nm in diffuse reflectance mode using a Varian (Agilent) Cary 5000 spectrophotometer. The surface morphology and composition of the  $\text{Sb}_2\text{S}_3$  films were analyzed using field emission scanning electron microscope (FESEM JSM 5400LV) equipped with a NORAN energy-dispersive X-ray spectrometer (EDS) attached to the FESEM. A Thermo Fisher Scientific K-Alpha X-ray photoelectron spectrometer with Al  $\text{K}\alpha$  (1487 eV) as the excitation source was used to examine the chemical state of the constituent present in the films. The photoconductivity measurement was done using an automated Keithley 230 voltage source and a Keithley 619 electrometer. Two planar carbon electrodes of 3 mm in length and separated by 5 mm were painted on the film surface using conductive graphite paint,

and light was illuminated from the top. Prior to the application of any voltage, the samples were kept in the dark for 30 min. Photocurrent response of the films was measured under a tungsten halogen lamp with an illumination intensity of 1000  $\text{W/m}^2$ .

## Results and discussion

### XRD study

Figure 1 shows the XRD patterns of undoped and Ag-doped  $\text{Sb}_2\text{S}_3$  films annealed at 300 °C. The standard patterns corresponding to the orthorhombic stibnite (JCPDS# 42-1393) and cubic senarmontite (JCPDS# 05-0534) structures are included for reference. In both cases, all the diffraction peaks are assigned to the planes of stibnite  $\text{Sb}_2\text{S}_3$  phase except two minor peaks at  $2\theta = 13.8^\circ$  and  $27.53^\circ$  which may belong to the (111) and (222) planes of senarmontite  $\text{Sb}_2\text{O}_3$  structure. For Ag-doped  $\text{Sb}_2\text{S}_3$  film, two low-

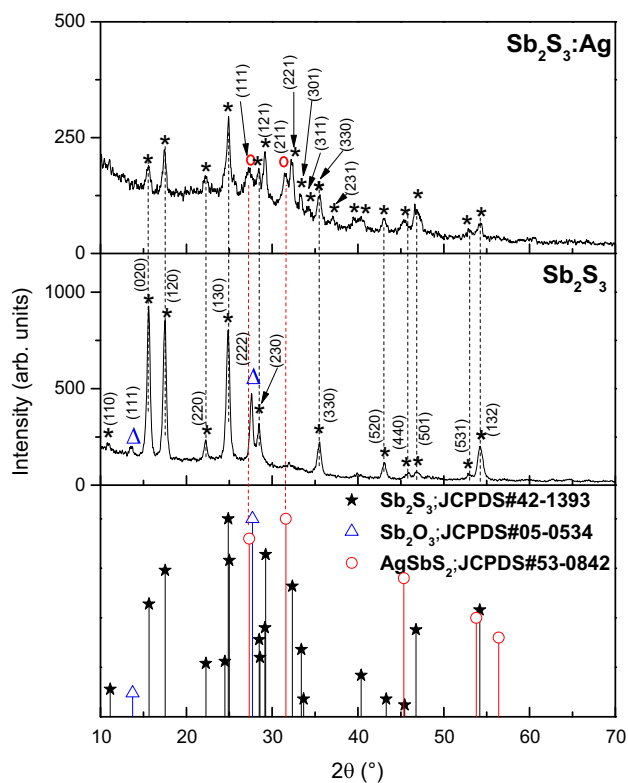


**Figure 1** XRD patterns of chemically deposited undoped and Ag-doped  $\text{Sb}_2\text{S}_3$  films annealed at 300 °C for 1 h. The reference patterns of stibnite  $\text{Sb}_2\text{S}_3$  (orthorhombic), cuboargyrite  $\text{AgSbS}_2$  (cubic) and senarmontite  $\text{Sb}_2\text{O}_3$  (cubic) phases are also included for the comparison.

intense peaks were observed at  $2\theta$  values  $27.34^\circ$  and  $31.58^\circ$ , which can be attributed to (111) and (200) planes of cuboargyrite  $\text{AgSbS}_2$  phase (JCPDS# 53-0842). No peak corresponding to metallic Ag was detected suggesting that it may be present at low concentration which is below the detection limit of XRD instrument or it is present as amorphous phase. In addition, the intensity of XRD peaks decreases drastically in the doped films along with an increment in peak width which is mainly due to the lower crystallinity of the film compared to the undoped one. The larger size of dopant ions compared to  $\text{Sb}^{3+}$  (ionic radius of  $\text{Sb}^{3+}$  and  $\text{Ag}^+$  ions is 0.74 and 1.26 Å, respectively) causes several lattice defects and distortion of  $\text{Sb}_2\text{S}_3$  unit cell [15]. Similar observation has been reported for Sn-doped  $\text{TiO}_2$  nanoparticles used as photoanode in dye sensitized solar [22] and Ag-doped ZnO films [23]. In the undoped film, the intensity of (020), (120) and (130) reflections is higher compared to the other planes, while for Ag-doped  $\text{Sb}_2\text{S}_3$ , the intensity of (020) and (120) decreases being the (130) is of highest intensity. This suggests that Ag doping causes a significant reduction in the preferential orientation of (020) and (120) planes in the doped films.

To get further information about the microstructure of the films, we have calculated several parameters like crystallite size, crystal strain and dislocation density based on the XRD patterns. The average crystallite size ( $D$ ) of the grains in the films was estimated from the broadening of the three prominent peaks, (020), (120) and (130) with the help of Scherrer's equation and taking the average of the three values:

$$D = 0.9\lambda/\beta \cos \theta \tag{1}$$

where  $\lambda$  is the X-ray wavelength,  $\beta$  is the full width at half-maximum of the diffraction peaks under consideration, and  $\theta$  is the Bragg angle.

The lattice strain ( $\varepsilon$ ) was calculated for undoped and Ag-doped  $\text{Sb}_2\text{S}_3$  films using the Scherrer's relation:

$$\varepsilon = \beta / \tan \theta \tag{2}$$

The dislocation density ( $\delta$ ) caused by Ag doping was evaluated using the formula:

$$\delta = 1/D^2 \tag{3}$$

The average crystallite size for  $\text{Sb}_2\text{S}_3$  film was found to decrease from 19.3 to  $\sim 17$  nm on Ag

doping, while the crystal strain was found to increase from  $10.5 \times 10^{-3}$  to  $12.2 \times 10^{-3}$ . We assume that due to the larger ionic radius of Ag ion, the growth of  $\text{Sb}_2\text{S}_3$  crystallites are inhibited to some extent leading to the smaller grain size and the higher lattice strain in the doped films compared to the undoped one.

The lattice parameters for undoped and Ag-doped  $\text{Sb}_2\text{S}_3$  thin films were calculated by using the following equation for the orthorhombic system ( $a \neq b \neq c$ ):

$$\frac{1}{d_{hkl}^2} = \frac{h^2}{a^2} + \frac{k^2}{b^2} + \frac{l^2}{c^2} \tag{4}$$

where  $d$  is interplanar spacing determined using Bragg's equation and  $h, k, l$  are the miller indices of the lattice planes. The calculated values of lattice parameters and other microstructural parameters are tabulated in Table 1. The lattice parameter,  $a$ , of the unit cell is found to decrease from 11.273 to 10.846 Å while  $b$  is found to undergo an increment from 11.353 to 11.422 Å on doping. On the other hand, the lattice parameter  $c$  was not changed considerably on doping. The observed change in lattice parameters can be attributed to the incorporation of Ag into  $\text{Sb}_2\text{S}_3$  matrix where the difference in size between dopant and host ions is considerably large.

The texture coefficient, TC ( $hkl$ ), was calculated for the main planes using the following expression:

$$TC(hkl) = \frac{\frac{I(hkl)}{I_0(hkl)}}{\sum_N \frac{I(hkl)}{I_0(hkl)}} N \tag{5}$$

where  $I_0(hkl)$  is the standard intensity of the plane,  $I(hkl)$  is the observed intensity of the ( $hkl$ ) plane, and  $N$  is the number of diffraction peaks. The results of TC calculated from integrated intensity ratios for respective Miller indices are shown in Table 2.

It is known that an increase in the TC with respect to unity implies a higher degree of preferred orientation along a particular plane. On the other hand, the deviation in texture coefficient from unity for a particular plane indicates the change in atomic densities for that particular Miller plane [24]. Therefore, an increment in TC implies an increase in planar density along a specified plane and vice versa. The results indicate that the undoped film is highly textured along (020) plane, while the Ag-doped films show a significant increase in TC from 0.813 to 1.117 along (130) with a concomitant decrease in TC along (020) plane. Therefore, texture analysis reveals that the

**Table 1** Microstructural parameter calculated for doped and undoped  $\text{Sb}_2\text{S}_3$  films

| Sample                            | $D$ (nm) | $\varepsilon$         | $\delta$ ( $\text{nm}^{-2}$ ) | Lattice parameters ( $\text{\AA}$ ) |        |       |
|-----------------------------------|----------|-----------------------|-------------------------------|-------------------------------------|--------|-------|
|                                   |          |                       |                               | $a$                                 | $b$    | $c$   |
| $\text{Sb}_2\text{S}_3$           | 19.32    | $10.5 \times 10^{-3}$ | $2.68 \times 10^{-3}$         | 11.273                              | 11.353 | 3.843 |
| $\text{Sb}_2\text{S}_3:\text{Ag}$ | 16.98    | $12.2 \times 10^{-3}$ | $3.47 \times 10^{-3}$         | 10.846                              | 11.422 | 3.835 |

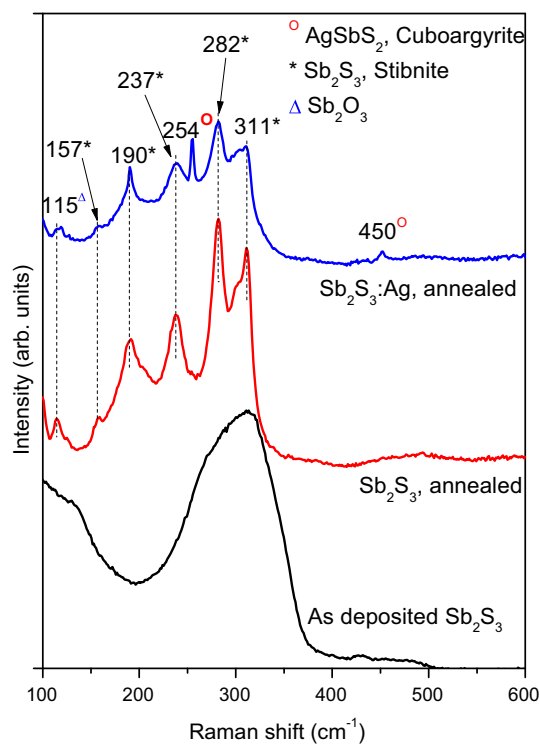
**Table 2** Texture coefficients calculated for pure and Ag-doped  $\text{Sb}_2\text{S}_3$  films

| Planes ( $hkl$ ) | Texture coefficient             |                                  |
|------------------|---------------------------------|----------------------------------|
|                  | Undoped $\text{Sb}_2\text{S}_3$ | Ag-doped $\text{Sb}_2\text{S}_3$ |
| (020)            | 1.644                           | 1.256                            |
| (120)            | 1.165                           | 1.155                            |
| (130)            | 0.813                           | 1.117                            |
| (132)            | 0.376                           | 0.470                            |

incorporation of Ag in  $\text{Sb}_2\text{S}_3$  lattice causes a considerable increase in planar density for (130) plane with a simultaneous decrease of (020) plane which in turn indicates that Ag doping creates many vacancies on (020) plane of  $\text{Sb}_2\text{S}_3$  unit cell.

### Raman scattering

To study the effect of Ag doping on Raman scattering properties of  $\text{Sb}_2\text{S}_3$  films, Raman spectral analysis was done and the spectra for undoped and Ag-doped  $\text{Sb}_2\text{S}_3$  films are shown in Fig. 2. In the case of as-deposited  $\text{Sb}_2\text{S}_3$  films, a broad peak centered at  $310 \text{ cm}^{-1}$  can be observed which is characteristic of amorphous phase of antimony sulfides. Upon annealing, well-defined and intense Raman peaks were observed at 190, 237, 282 and  $311 \text{ cm}^{-1}$  together with a weak band at  $157 \text{ cm}^{-1}$  for both undoped and Ag-doped  $\text{Sb}_2\text{S}_3$  films. These bands are in well agreement with the characteristic vibrational modes of stibnite  $\text{Sb}_2\text{S}_3$  phase. The peaks at 157, 190 and  $282 \text{ cm}^{-1}$  can be correlated to  $A_g$  modes and the peaks at 237 and  $311 \text{ cm}^{-1}$  are associated with  $B_{1g}$  vibrational modes [25, 26]. A small peak at  $115 \text{ cm}^{-1}$  can be assigned to senarmontite  $\text{Sb}_2\text{O}_3$  phase which is in agreement with XRD results [27]. In the presence of Ag dopants, Raman peaks become weaker and broader. Additionally, a peak at  $254 \text{ cm}^{-1}$  and its second harmonic mode at  $450 \text{ cm}^{-1}$  were observed which can be attributed to cuboargyrite phase of  $\text{AgSbS}_2$  which is in well agreement with XRD results. A similar report has been documented in the

**Figure 2** Raman spectra of undoped and Ag-doped  $\text{Sb}_2\text{S}_3$  films before and after annealing.

literature, indicating that the  $254 \text{ cm}^{-1}$  peak corresponds to Sb-S stretching vibrations of  $\text{SbS}_3$  pyramids in miargyrite phase of  $\text{AgSbS}_2$  [28]. The broadening of phonon modes and the concomitant decrease in intensity is due to the decrease in phonon correlation lengths caused by local crystal lattice disorder induced by doping [23].

### SEM analysis

The morphology of the  $\text{Sb}_2\text{S}_3$  films after annealing was studied using field emission scanning electron microscopy (FESEM), and images are presented in Fig. 3. In both cases, the dark background corresponds to either  $\text{Sb}_2\text{S}_3$  or  $\text{Sb}_2\text{S}_3:\text{Ag}$  film along with the irregular distribution of surface particles. In the case of undoped film, these aggregates are interconnected with each other and distributed all over the surface

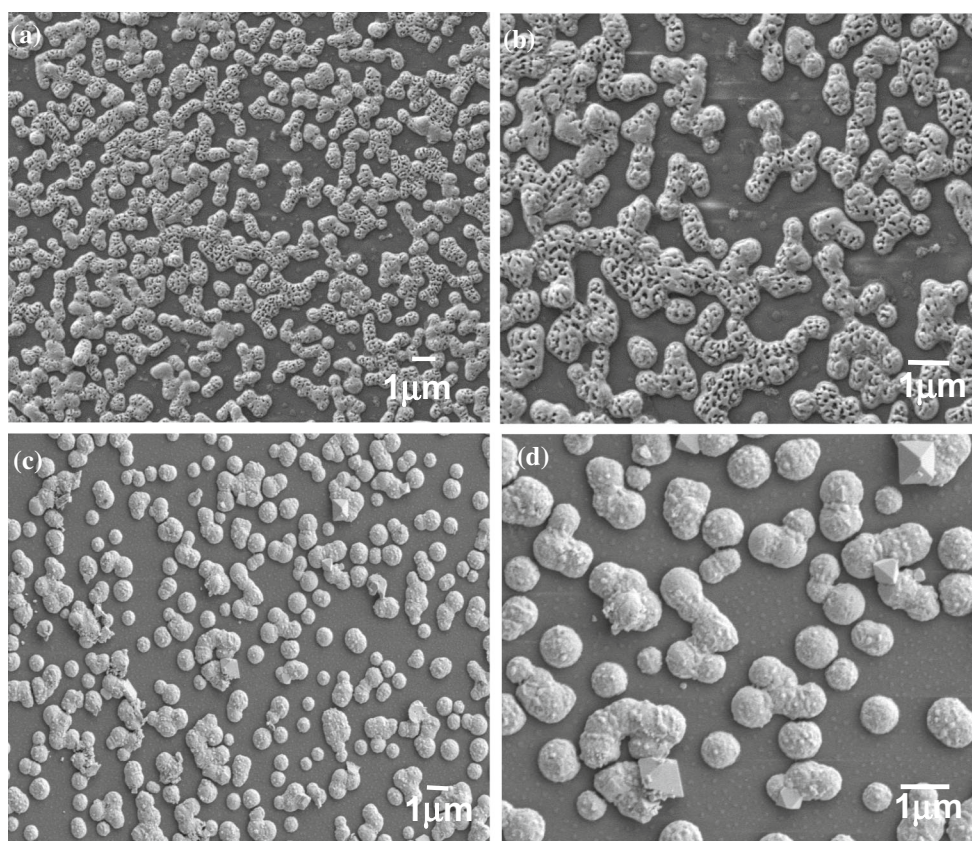


**Figure 3** SEM micrographs of  $\text{Sb}_2\text{S}_3$  films annealed at 300 °C for 1 h: **a, b** correspond to pure  $\text{Sb}_2\text{S}_3$  taken at 5000 and 10000 magnification, respectively. **c, d** Ag-doped  $\text{Sb}_2\text{S}_3$  films imaged at 5000 and 10,000 magnification.

while in the Ag-doped film, the clusters are more isolated as can be observed in Fig. 3a, b. The presence of unevenly distributed, agglomerated surface particles is reported to be a common morphological feature in chemical bath-deposited  $\text{Sb}_2\text{S}_3$  films [5]. The incorporation of Ag is found to decrease the number of surface particles forming a more homogenous film with slightly higher thickness; this can be associated with the formation of new nucleation centers due to Ag doping [29]. The octahedron-shaped crystallites shown in Fig. 3d corresponds to antimony oxide as evidenced by EDS analysis.

Semiquantitative chemical composition of undoped and Ag-doped  $\text{Sb}_2\text{S}_3$  thin films was measured by energy-dispersive X-ray spectroscopy. The atomic percentages of Sb and S are 36.83 and 63.17 in the undoped film, suggesting the films are slightly Sb-deficient. In the doped film, the presence of Ag has been detected as 7.25 at. %, while Sb and S are found to be present in the ratio of 35.32 and 57.43, respectively. EDS measurements performed on octahedron-shaped crystals result in the characteristic

emission peaks of Sb and O with an atomic percentage ratio of 27.84 and 72.16, respectively.

### XPS analysis

The XPS spectra were registered with a Thermo Fisher Scientific K-Alpha spectrometer using the  $\text{AlK}\alpha$  excitation line at 1487 eV. All the XPS signals were calibrated using the C1s peak at 284.6 eV resulting from the adventitious hydrocarbon. The peaks were deconvoluted using Shirley background method. For these measurements, we used an energy step size of 0.10 eV, a pass energy of 50 eV, and a spot size of 400 mm.

A detailed analysis of the chemical states was further carried out using X-ray photoelectron spectroscopy. Figure 4 shows the XPS survey scan from the surface of  $\text{Sb}_2\text{S}_3$  and  $\text{Sb}_2\text{S}_3:\text{Ag}$  thin film in a binding energy range of 0–1000 eV. The spectrum of the undoped film showed the characteristic peaks from Sb 3p, 3d, 4d and S 2p. In addition to Sb and S peaks, Ag-doped films showed the double Ag 3d

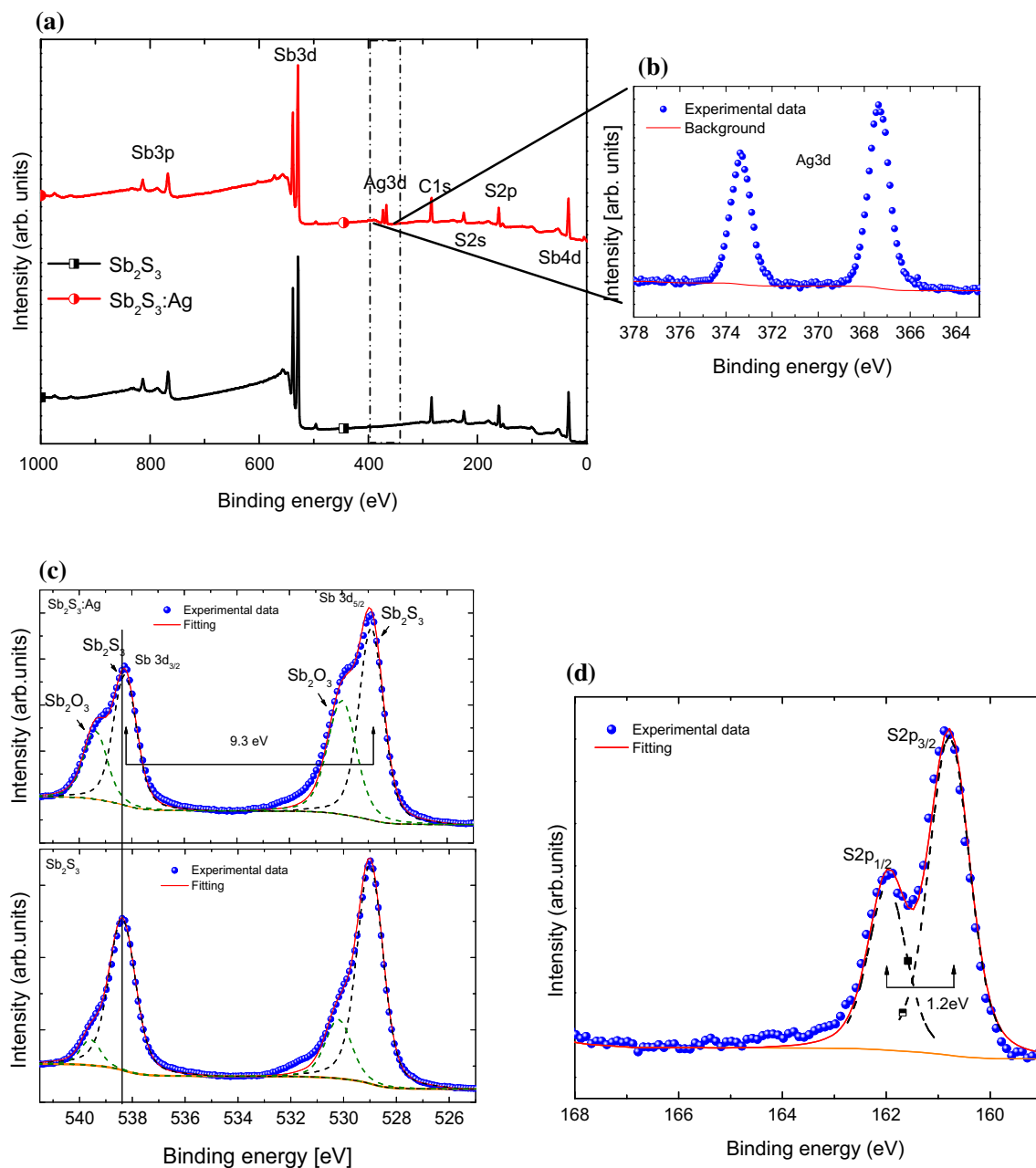


**Figure 4** a XPS survey spectra of undoped and Ag-doped  $\text{Sb}_2\text{S}_3$  films. High-resolution spectra of **b** Ag 3d spectrum, **c** Sb 3d spectrum of  $\text{Sb}_2\text{S}_3$  and  $\text{Sb}_2\text{S}_3:\text{Ag}$  thin films and **d** S 2p spectrum of

Ag-doped film. The experimental data, the fitting curve and deconvoluted peaks (dotted lines) are presented in the spectra.

peaks confirming the presence of Ag in the films. The C1s peak present in both samples can be presumably due to the contamination from the environment. The high-resolution XPS spectrum of Ag 3d (Fig. 4b) shows peaks at 373.29 and 367.37 eV corresponding to Ag  $3d_{5/2}$  and Ag  $3d_{3/2}$ , respectively, with a spin orbital separation of 5.92 eV which are characteristic of metallic Ag [30].

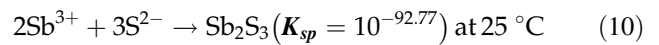
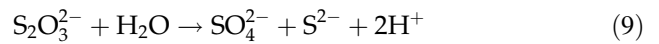
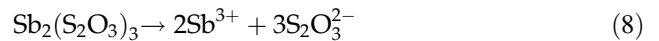
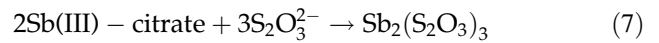
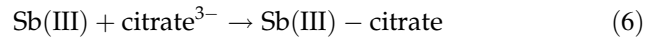
Figure 4c shows the high-resolution XPS spectra of Sb 3d core level obtained from  $\text{Sb}_2\text{S}_3$  and  $\text{Sb}_2\text{S}_3:\text{Ag}$  films. The experimental spectra and the deconvoluted ones (dotted) are included in the figure. The Sb  $3d_{3/2}$  and Sb  $3d_{5/2}$  shows two distinct peaks, indicating the presence of Sb in different environments. The  $\text{Sb}_2\text{S}_3$  and  $\text{Sb}_2\text{S}_3:\text{Ag}$  have identical Sb 3d peak positions. The high-intense peaks at 538.28 and 528.88 eV with a

separation of 9.4 eV coincide well with Sb 3d<sub>3/2</sub> and Sb 3d<sub>5/2</sub> of Sb<sup>3+</sup> in Sb<sub>2</sub>S<sub>3</sub> [31, 32]. The low-intense peaks at slightly higher binding energies, 539.38 and 529.98 can be matched with Sb<sup>3+</sup> in Sb<sub>2</sub>O<sub>3</sub> [33, 34]. The presence of Sb<sub>2</sub>O<sub>3</sub> is evident in X-ray analysis also. The high-resolution core level spectrum of S2p doublets is given in Fig. 4d. The deconvoluted peaks are located at 161.98 and 160.78 eV with a doublet separation of 1.2 eV which correspond to the binding energy values of S2p<sub>3/2</sub> and S2p<sub>1/2</sub>, respectively. These values are in agreement with the S in metal sulfides (S<sup>2-</sup>), in our case of S-Sb bond in Sb<sub>2</sub>S<sub>3</sub> [35].

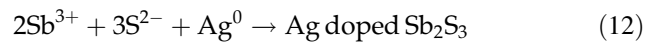
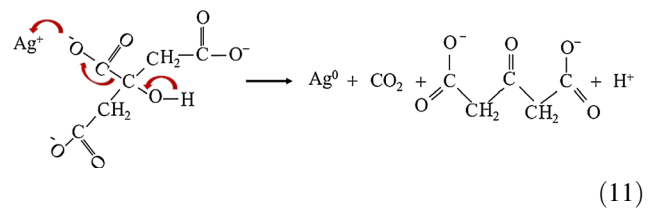
### Formation mechanism

CBD was used to deposit Sb<sub>2</sub>S<sub>3</sub> thin films from an aqueous solution containing Sb-salt, ethylene glycol, sodium thiosulfate and sodium citrate. One of the difficulties in the use of Sb salts in aqueous solution arises from the strong tendency of Sb salts to hydrolyze in water and precipitate as insoluble hydroxyl salts. In the present case, Sb (III) chloride was dissolved in a small amount of ethylene glycol and then complexed by aqueous solution of sodium citrate. The intention to use ethylene glycol as solvent instead of widely used acetone for SbCl<sub>3</sub> is to maintain reducing atmosphere and prevents the oxidation of metallic ions. The pH of the citrate complexed Sb-solution was determined to be ~ 1.5. After the addition of sodium thiosulfate as sulfur precursor, the pH of the solution was increased to ~ 5 and citrate species were gradually replaced by thiosulfate ions forming a complex between Sb<sup>3+</sup> and S<sub>2</sub>O<sub>3</sub><sup>2-</sup> ions. The resulting antimony (III)-thiosulfate complex was further dissociated into Sb(III) and thiosulfate ions. At acidic medium, the thiosulfate ions were further hydrolyzed to release sulfide ions (S<sup>2-</sup>). Finally, Sb<sup>3+</sup> and S<sup>2-</sup> ions released by the above reactions condense on the surface of the substrate to form Sb<sub>2</sub>S<sub>3</sub>. In this growth mechanism, sodium citrate not only acts as a complexing agent and maintains control over the free antimony ions in solution but also serves as a buffer. Usually, Sb<sup>3+</sup> ions tend to precipitate as Sb<sub>2</sub>O<sub>3</sub> in neutral or less acidic solution. However, the resulting complexation of Sb<sup>3+</sup> by citrate species and the buffering action of sodium citrate prevent the formation of antimony oxide to large extent [36]. In the case of Ag-doped Sb<sub>2</sub>S<sub>3</sub>, the Ag<sup>+</sup> ions become reduced to Ag<sup>0</sup> by sodium citrate which acts as reductant. The electropositive reduction potential of Ag<sup>+</sup> → Ag<sup>0</sup> in water with E<sup>0</sup> = +0.799 V

allows the use of sodium citrate as a reducing agent (E<sup>0</sup> = - 0.230 V). It has also been reported that under equimolar conditions of [citrate]/[Ag<sup>+</sup>], a fraction of Ag<sup>+</sup> was not reduced [37]. As in our synthesis, the molar ratio of [citrate]/[Ag<sup>+</sup>] >>>1, all the Ag<sup>+</sup> are expected to be reduced to Ag<sup>0</sup> as evidenced by XPS results. The following set of chemical reactions describes the formation of Sb<sub>2</sub>S<sub>3</sub> and Ag-doped Sb<sub>2</sub>S<sub>3</sub> by CBD method:



For Ag doping:



### Optical properties

The diffuse reflectance absorbance spectra of undoped and Ag-doped films are shown in Fig. 5a. As it can be seen, there is an absorption onset at around 750 nm for undoped Sb<sub>2</sub>S<sub>3</sub> film which has been red-shifted to 800 nm on Ag doping. The absorption capacity of the films in the wavelength range of 600–800 nm suggests the visible light sensitivity of the films. The UV–Vis diffuse reflectance spectra of Sb<sub>2</sub>S<sub>3</sub> films are shown in inset of Fig. 5b. The reflectance spectra have been converted into absorbance data using Kubelka–Munk function

$$F(R_\infty) = \frac{(1 - R_\infty)^2}{2R_\infty} \quad (13)$$

$$R_\infty = \frac{R_{\text{sample}}}{R_{\text{standar}}} \quad (14)$$

where F(R<sub>∞</sub>) is the Kubelka–Munk function and R is the reflectance. The optical band gap of Sb<sub>2</sub>S<sub>3</sub> films



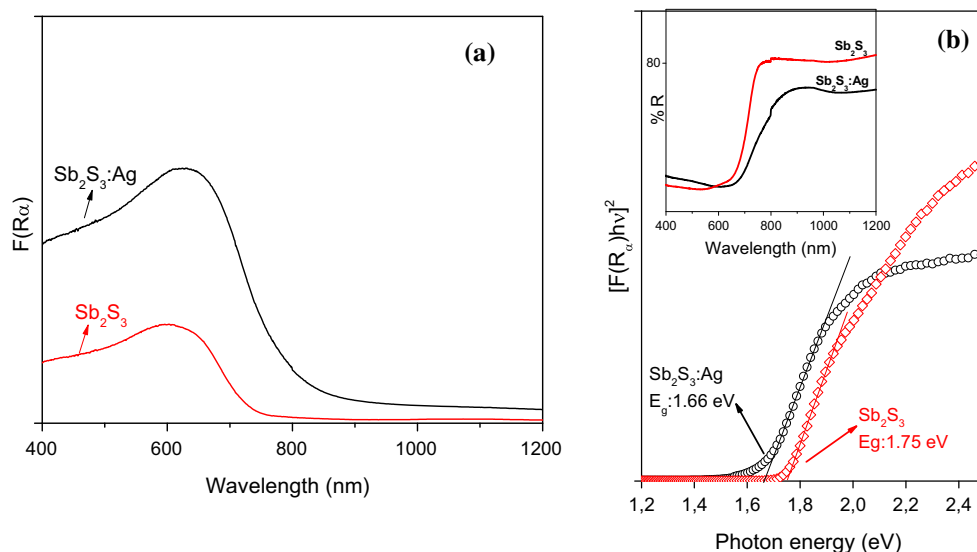


**Figure 5** **a** Diffuse reflectance absorbance spectra of undoped and Ag-doped  $\text{Sb}_2\text{S}_3$  film. **b** Plot of  $[F(R_\infty)hv]^2$  versus  $(hv)$  of  $\text{Sb}_2\text{S}_3$  films showing a decrease in band gap on Ag doping. Inset shows the diffuse reflectance spectra of  $\text{Sb}_2\text{S}_3$  films.

was calculated from  $F(R_\infty)$  using the following equation associated with the direct transition:

$$F(R_\infty) = A(h\nu - E_g)^{1/2} \quad (15)$$

where  $h\nu$  is the photon energy,  $A$  is a constant and  $E_g$  is the band gap. The curves of  $[F(R_\infty)hv]^2$  versus  $(h\nu)$  for the films are plotted in Fig. 5b. By extrapolating the linear portion of the  $[F(R_\infty)hv]^2$  versus  $(h\nu)$  curves to photon energy axis, the  $E_g$  values of  $\text{Sb}_2\text{S}_3$  and  $\text{Sb}_2\text{S}_3:\text{Ag}$  films were determined as 1.75 and 1.66 eV, respectively. The red shift in absorption onset from 750 to 800 nm in Ag-doped  $\text{Sb}_2\text{S}_3$  is due to the interaction between 3d level of Ag and the valence band of  $\text{Sb}_2\text{S}_3$  matrix which obviously causes a significant band gap narrowing on doping. Similar observations have been reported by Gong et al. for Ag-doped Zn–In–S quantum dots where by increasing the Ag (dopant) concentration from 0 to 3 mol%, the band gap could be adjusted from 3.28 to 2.01 eV [38].

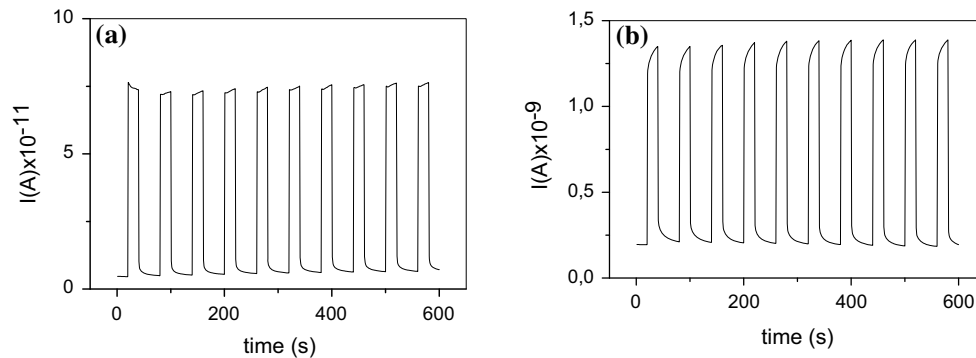
### Photoconductivity

Figure 6 shows the cyclic photoresponse curves of  $\text{Sb}_2\text{S}_3$  and  $\text{Sb}_2\text{S}_3:\text{Ag}$ -doped films. The current was collected at a constant applied bias of 20 V, first 40 s in dark, then 20 s in light and again 40 s in dark. Multiple cycles were done to evaluate the photostability of the films, and as can be seen from the figure the films were photosensitive (current variation

with illumination) and stable. The dark and light conductivities of  $\text{Sb}_2\text{S}_3$  films were  $1.84 \times 10^{-9}$  and  $1.11 \times 10^{-7} (\Omega \text{ cm})^{-1}$ , respectively. This indicates two orders of increase in conductivity under illumination. When doped with Ag, the dark conductivity of  $\text{Sb}_2\text{S}_3$  films was found to increase, from  $1.84 \times 10^{-9} (\Omega \text{ cm})^{-1}$  to  $1.33 \times 10^{-8} (\Omega \text{ cm})^{-1}$  showing a possible incorporation of Ag. The photosensitivity was calculated as  $S_{ph} = (I_L - I_D)/I_D$  where  $I_L$  and  $I_D$  are the illuminated and dark currents, respectively. The  $S_{ph}$  is 65 and 12 for undoped and doped thin films, respectively. Both the conductivity and photosensitivity values are in good agreement with the values reported for chemical bath-deposited  $\text{Sb}_2\text{S}_3$  films in the literature [25, 39, 40]. The decrease in photosensitivity with Ag doping could be associated with the increase in the dark conductivity due to the introduction of silver ions. Another important feature is the nature of current fall once light is switched off;  $\text{Sb}_2\text{S}_3$  shows a sharp decrease (Fig. 6a), whereas  $\text{Sb}_2\text{S}_3:\text{Ag}$  shows a slow decay (Fig. 6b). This slow decay can be attributed to the presence of charge trap centers in the band gap of  $\text{Sb}_2\text{S}_3$  films doped with Ag.

### Conclusion

In this work, the effect of Ag ion incorporation on some physical properties of the  $\text{Sb}_2\text{S}_3$  thin films has been studied systematically. XRD and Raman studies



**Figure 6** Cyclic photocurrent response of  $\text{Sb}_2\text{S}_3$  films after annealing at 300 °C for 1 h in  $\text{N}_2$  atmosphere: **a** without doping and **b** with 7.5 mol% Ag doping.

revealed the incorporation of Ag in  $\text{Sb}_2\text{S}_3$  host lattice without altering the crystal structure. The calculated crystallite size was decreased; meanwhile, the lattice stress and dislocation density were increased on doping. Ag incorporation was found to improve the morphological properties of the  $\text{Sb}_2\text{S}_3$  films being the films more uniform and dense. Both films are found to be photoactive in visible spectral range with a slight decrease in the band gap values on doping. XPS analysis confirms the presence of metallic Ag in  $\text{Sb}_2\text{S}_3$  lattice. A possible reason has been put forward for the incorporation of metallic Ag and not Ag ions into the  $\text{Sb}_2\text{S}_3$  lattice. Electrical measurements indicate that the dark conductivity was increased by one order on silver doping, and both films are photosensitive.

## Acknowledgements

The authors are sincerely thankful to Dr. R. Silva Gonzalez for extending the facilities for SEM and EDS measurements. The authors acknowledge the grants received through the projects CONACyT-DST Bilateral 2015 (#266406) & PAPIIT (IN107815). Dr. C. J. Diliégros-Godines acknowledges the postdoctoral fellowship obtained through SEP-PRODEP (# 511-6/18-829).

## Compliance with ethical standards

**Conflict of interest** The authors declare no conflict of interest.

## References

- [1] Varghese J, Barth S, Keeney L, Whatmore RW, Holmes JD (2012) Nanoscale ferroelectric and piezoelectric properties of  $\text{Sb}_2\text{S}_3$  nanowire arrays. *Nano Lett* 12:868–872. <https://doi.org/10.1021/nl2039106>
- [2] Chao J, Liang B, Hou X et al (2013) Selective synthesis of  $\text{Sb}_2\text{S}_3$  nanoneedles and nanoflowers for high performance rigid and flexible photodetectors. *Opt Express* 21:13639–13647. <https://doi.org/10.1364/OE.21.013639>
- [3] Yesugade NS, Lokhande CD, Bhosale CH (1995) Structural and optical properties of electrodeposited  $\text{Bi}_2\text{S}_3$ ,  $\text{Sb}_2\text{S}_3$  and  $\text{As}_2\text{S}_3$  thin films. *Thin Solid Films* 263:145–149. [https://doi.org/10.1016/0040-6090\(95\)06577-6](https://doi.org/10.1016/0040-6090(95)06577-6)
- [4] Aousgi F, Kanzari M (2011) Study of the optical properties of Sn-doped  $\text{Sb}_2\text{S}_3$  thin films. *Energy Proc* 10:313–322. <https://doi.org/10.1016/j.egypro.2011.10.197>
- [5] Krishnan B, Arato A, Cardenas E, Das Roy TK, Castillo GA (2008) On the structure, morphology, and optical properties of chemical bath deposited  $\text{Sb}_2\text{S}_3$  thin films. *Appl Surf Sci* 254:3200–3206. <https://doi.org/10.1016/j.apsusc.2007.10.098>
- [6] Gil EK, Lee SJ, Sung SJ, Cho KY, Kim DH (2016) Spin-coating process of an inorganic  $\text{Sb}_2\text{S}_3$  thin film for photovoltaic applications. *J Nanosci Nanotechnol* 16:10763–10766. <https://doi.org/10.1166/jnn.2016.13235>
- [7] Savadogo O, Mandal KC (1994) Low cost Schottky barrier solar cells fabricated on CdSe and  $\text{Sb}_2\text{S}_3$  films chemically deposited with silicotungstic acid. *J Electrochem Soc* 141:2871–2877. <https://doi.org/10.1149/1.2059248>
- [8] Abulikemu M, Del Gobbo S, Anjum DH, Malik MA, Bakr OM (2016) Colloidal  $\text{Sb}_2\text{S}_3$  nanocrystals: synthesis, characterization and fabrication of solid-state semiconductor sensitized solar cells. *J Mater Chem A* 4:6809–6814. <https://doi.org/10.1039/C5TA09546H>

- [9] Itzhaik Y, Niiitsoo O, Page M, Hodes G (2009) Sb<sub>2</sub>S<sub>3</sub>-sensitized nanoporous TiO<sub>2</sub> solar cells. *J Phys Chem C* 113:4254–4256. <https://doi.org/10.1021/jp900302b>
- [10] Cardoso JC, Grimes CA, Feng X et al (2012) Fabrication of coaxial TiO<sub>2</sub>/Sb<sub>2</sub>S<sub>3</sub> nanowire hybrids for efficient nanostructured organic–inorganic thin film photovoltaics. *Chem Commun* 48:2818–2820. <https://doi.org/10.1039/c2cc17573h>
- [11] Moon SJ, Itzhaik Y, Yum JH et al (2010) Sb<sub>2</sub>S<sub>3</sub>-Based mesoscopic solar cell using an organic hole conductor. *J Phys Chem Lett* 1:1524–1527. <https://doi.org/10.1021/jz100308q>
- [12] DeAngelis AD, Kemp KC, Gaillard N, Kim KS (2016) Antimony (III) sulfide thin Films as a photoanode material in photocatalytic water splitting. *ACS Appl Mater Interfaces* 8:8445–8451. <https://doi.org/10.1021/acsami.5b12178>
- [13] Choi YC, Seok SI (2015) Efficient Sb<sub>2</sub>S<sub>3</sub>-sensitized solar cells via single-step deposition of Sb<sub>2</sub>S<sub>3</sub> using S/Sb-ratio-controlled SbCl<sub>3</sub>-thiourea complex solution. *Adv Funct Mater* 25:2892–2898. <https://doi.org/10.1002/adfm.201500296>
- [14] Karguppikar AM, Vedeshwar AG (1987) Thickness dependence of the forbidden energy gap in stibnite (Sb<sub>2</sub>S<sub>3</sub>) thin films. *Phys Lett A* 126:123–126. [https://doi.org/10.1016/0375-9601\(87\)90570-6](https://doi.org/10.1016/0375-9601(87)90570-6)
- [15] Salim SM, Seddek MB, Salem, Islam AM (2010) Low-temperature synthesis of Ag-doped Sb<sub>2</sub>S<sub>3</sub> thin films and its characterization. *Appl Sci Res* 6:1352–1358
- [16] Dong W, Krbal M, Kalikka J et al (2016) Enhanced Sb<sub>2</sub>S<sub>3</sub> crystallisation by electric field induced silver doping. *Thin Solid Films* 616:80–85. <https://doi.org/10.1016/j.tsf.2016.07.068>
- [17] Mushtaq S, Ismail B, Aurang Zeb M, Suthan Kissinger NJ, Zeb A (2015) Low-temperature synthesis and characterization of Sn-doped Sb<sub>2</sub>S<sub>3</sub> thin film for solar cell applications. *J Alloys Compd* 632:723–728. <https://doi.org/10.1016/j.jallcom.2015.01.307>
- [18] Cárdenas E, Arato A, Perez-Tijerina E, Das Roy TK, Alan Castillo G, Krishnan B (2009) Carbon-doped Sb<sub>2</sub>S<sub>3</sub> thin films: structural, optical and electrical properties. *Sol Energy Mater Sol Cells* 93:33–36. <https://doi.org/10.1016/j.solmat.2008.02.026>
- [19] Mushtaq S, Ismail B, Raheel M, Zeb A (2016) Nickel antimony sulphide thin films for solar cell application: study of optical constants. *Nat Sci* 8:33–40. <https://doi.org/10.4236/ns.2016.82004>
- [20] Mitkova M, Sakaguchi Y, Tenne D, Bhagat SK, Alford TL (2010) Structural details of Ge-rich and silver-doped chalcogenide glasses for nanoionic nonvolatile memory. *Phys Status Solidi Appl Mater Sci* 207:621–626. <https://doi.org/10.1002/pssa.200982902>
- [21] Kosa TI, Rangel-Rojo R, Hajto E et al (1993) Nonlinear optical properties of silver-doped As<sub>2</sub>S<sub>3</sub>. *J Non Cryst Solids* 164–166:1219–1222. [https://doi.org/10.1016/0022-3093\(93\)91220-W](https://doi.org/10.1016/0022-3093(93)91220-W)
- [22] Duan Y, Fu N, Liu Q et al (2012) Sn-doped TiO<sub>2</sub> photoanode for dye-sensitized solar cells. *J Phys Chem C* 116:8888–8893. <https://doi.org/10.1071/CH11031>
- [23] Wang XB, Song C, Geng KW, Zeng F, Pan F (2006) Luminescence and Raman scattering properties of Ag-doped ZnO films. *J Phys D Appl Phys* 39:4992–4996. <https://doi.org/10.1088/0022-3727/39/23/014>
- [24] Kumar M, Kumar A, Abhyankar AC (2015) Influence of texture coefficient on surface morphology and sensing properties of W-doped nanocrystalline tin oxide thin films. *ACS Appl Mater Interfaces* 7:3571–3580. <https://doi.org/10.1021/am507397z>
- [25] Shaji S, Garcia LV, Loredó SL et al (2017) Antimony sulfide thin films prepared by laser assisted chemical bath deposition. *Appl Surf Sci* 393:369–376. <https://doi.org/10.1016/j.apsusc.2016.10.051>
- [26] Pal M, Mathews NR, Mathew X (2017) Surfactant-mediated self-assembly of Sb<sub>2</sub>S<sub>3</sub> nanorods during hydrothermal synthesis. *J Mater Res* 32:530–538. <https://doi.org/10.1557/jmr.2016.470>
- [27] Makreski P, Petruševski G, Ugarković S, Jovanovski G (2013) Laser-induced transformation of stibnite (Sb<sub>2</sub>S<sub>3</sub>) and other structurally related salts. *Vib Spectrosc* 68:177–182. <https://doi.org/10.1016/j.vibspec.2013.07.007>
- [28] Galdámez A, López-Vergara F, Veloso Cid N et al (2014) Copper substitutions in synthetic miargyrite α-AgSbS<sub>2</sub> mineral: synthesis, characterization and dielectrical properties. *Mater Chem Phys* 143:1372–1377. <https://doi.org/10.1016/j.matchemphys.2013.11.048>
- [29] Sarica E, Bilgin V (2017) Study of some physical properties of ultrasonically spray deposited silver doped lead sulphide thin films. *Mater Sci Semicond Process* 68:288–294. <https://doi.org/10.1016/j.mssp.2017.06.034>
- [30] Gedi S, Minnam Reddy VR, Reddy Kotte TR, Kim SH, Jeon CW (2016) Chemically synthesized Ag-doped SnS films for PV applications. *Ceram Int* 42:19027–19035. <https://doi.org/10.1016/j.ceramint.2016.09.059>
- [31] Han Q, Chen L, Zhu W et al (2009) Synthesis of Sb<sub>2</sub>S<sub>3</sub> peanut-shaped superstructures. *Mater Lett* 63:1030–1032. <https://doi.org/10.1016/j.matlet.2009.01.078>
- [32] Avilez Garcia RG, Meza Avendaño CA, Pal M, Paraguay Delgado F, Mathews NR (2016) Antimony sulfide (Sb<sub>2</sub>S<sub>3</sub>) thin films by pulse electrodeposition: effect of thermal treatment on structural, optical and electrical properties.

- Mater Sci Semicond Process 44:91–100. <https://doi.org/10.1016/j.mssp.2015.12.018>
- [33] Moulder J, Stickie W, Sobal P, Bombier K (1992) Handbook of X-ray photoelectron spectroscopy. Perkin Elmer, Eden Prairie
- [34] Deng Z, Chen D, Tang F, Ren J, Muscat AJ (2009) Synthesis and purple-blue emission of antimony trioxide single-crystalline nanobelts with elliptical cross section. Nano Res 2:151–160. <https://doi.org/10.1007/s12274-009-9014-y>
- [35] Ornelas-Acosta RE, Shaji S, Avellaneda D, Castillo GA, Das Roy TK (2015) Thin films of copper antimony sulfide: a photovoltaic absorber material. Mater Res Bull 61:215–225. <https://doi.org/10.1016/j.materresbull.2014.10.027>
- [36] Loranca-Ramos FE, Diliegros-Godines CJ, Silva González R, Pal M (2018) Structural, optical and electrical properties of copper antimony sulfide thin films grown by a citrate-assisted single chemical bath deposition. Appl Surf Sci 427:1099–1106. <https://doi.org/10.1016/j.apsusc.2017.08.027>
- [37] Pillai ZS, Kamat PV (2004) What factors control the size and shape of silver nanoparticles in the citrate ion reduction method? J Phys Chem B 108:945–951. <https://doi.org/10.1021/jp037018r>
- [38] Gong G, Liu Y, Mao B, Tan L, Yang Y, Shi W (2017) Ag doping of Zn-In-S quantum dots for photocatalytic hydrogen evolution: simultaneous bandgap narrowing and carrier lifetime elongation. Appl Catal B Environ 216:11–19. <https://doi.org/10.1016/j.apcatb.2017.05.050>
- [39] Sotelo Marquina RG, Sanchez TG, Mathews NR, Mathew X (2017) Vacuum coated Sb<sub>2</sub>S<sub>3</sub> thin films: thermal treatment and the evolution of its physical properties. Mater Res Bull 90:285–294. <https://doi.org/10.1016/j.materresbull.2017.03.013>
- [40] Desai JD, Lokhande CD (1994) Alkaline bath chemical deposition of antimony (III) sulphide thin films. Thin Solid Films 237:29–31. [https://doi.org/10.1016/0040-6090\(94\)90234-8](https://doi.org/10.1016/0040-6090(94)90234-8)